Production and Incorporation of Calcium Hydrolyzed Nano-particles in Alkali-Activated Mine Tailings

Yibran Perera-Mercado [1,*], Nan Zhang [1], Ahmadreza Hedayat [1], Linda Figueroa [1], Esmeralda Saucedo-Salazar [2], Cara Clements [1], Héctor Gelber Bolaños Sosa[3], Néstor Tupa [3], Isaac Yanqui Morales [3], Reynaldo Sabino Canahua Loza [3]

[1] Department of Civil and Environmental Engineering, Colorado School of Mines, 1500 Illinois St., Golden, CO 8040, US.; hedayat@mines.edu (A.H.); caraclements@mines.edu (C.C.); lfiguero@mines.edu (L.F.); zhangnan@mines.edu (N.Z.)
[2] Centro de Investigación en Química Aplicada (CIQA), Blvd. Enrique Reyna Hermosillo 140, C.P. 25294, Saltillo, Coahuila, México; esmeralda.saucedo@ciqa.edu.mx (E.S.-S.)
[3] Universidad Nacional de San Agustín de Arequipa, Arequipa, Arequipa, Perú. hbolanos@unsa.edu.pe (H.G.B.S.); ntupaf@unsa.edu.pe (N.T.); iyanqui@unsa.edu.pe (I.Y.M.); rcanahua@unsa.edu.pe (R.S.C.L.)
* Correspondence: yibranpereramercado@gmail.com (Y.P.-M.)

Abstract: This work presents the production and incorporation of calcium hydrolyzed nano-solutions at three concentrations (1, 2, and 3 wt.%) in alkali-activated gold mine tailings (MTs) from Arequipa, Perú. A first activator solution of sodium hydroxide (NaOH) at 10M was used. The calcium hydrolyzed nano-solutions acted as a secondary activator and as additional calcium resource for the alkali-activated materials (AAMs) based on the low-calcium gold MTs. High-resolution transmission electron microscopy/energy-dispersive x-ray spectroscopy (HR-TEM/EDS) analyses were carried out to characterize the morphology, size, and structures of the calcium hydrolyzed nanoparticles. Fourier transform infrared (FTIR) analyses were then used to understand the chemical bonding interactions in the calcium hydrolyzed nanoparticles and in the AAMs. Scanning electron microscopy/energy-dispersive X-ray spectroscopy (SEM/EDS) and Quantitative X-ray diffraction (QXRD) were performed to study the structural, chemical, and phase compositions of the AAMs; uniaxial compressive tests evaluated the compressive strength of the reacted AAMs; and Nitrogen adsorption-desorption analyses measured the porosity changes at nanostructure level in the AAMs. The results indicate that each increase in the concentration of the calcium hydrolyzed nano-solution had a direct/proportional effect on the mechanical properties of the AAMs samples. The AAMs with 3 wt.% calcium-hydrolyzed nano-solution had the highest compressive strength value of 15.16 MPa, which represented an increase of 62% compared to the original system without nanoparticles and aged under the same conditions of 70°C for seven days. These results provide useful information about the positive effect of calcium-hydrolyzed nanoparticles on gold MTs and their conversion into sustainable building materials through alkali activation.

Keywords: Sol-gel; surfactant; nanoparticles; calcium hydroxide; nano-solutions; alkali-activated materials.

1. Introduction

The mining industry generates significant quantities of mine tailings (MTs) with an estimated total annual amount of over 7 billion tons globally [1]. The repurposing option of mine tailings in the form of building materials is very attractive and yet relatively unexplored. Furthermore, the alternative eco-efficient binders for producing construction composites developed primarily from industrial wastes such as MTs are promising to address their global solid waste management goals. In this respect, alkali-activated materials (AAMs) and geopolymer-based systems are considered as alternative potential candidates to the ordinary Portland cement systems [2],[3].

 doi:10.20944/preprints202304.1079.v1

According to Provis [4], alkali activation is the generic term which is applied to the reaction of a solid aluminosilicate (precursor) under alkaline conditions (activator), to produce a hardened binder which is based on a combination of hydrous alkali-aluminosilicate and/or alkali-alkali earth-aluminosilicate phases [4]. Therefore, AAMs can be produced by mixing silicon and aluminum rich raw materials with highly alkaline solution. Silicon and aluminum will be released into the solution in high pH conditions and start to form a new three-dimensional concrete like hardened structure with high mechanical and chemical performance. Besides the Si and Al, elements such as Fe, Mg and Ca, can react in the matrix formation producing other solid phases, which can affect the final properties of the structure [1]. In addition, the widely used term geopolymers in fact refers to a subclass of AAMs (although a general consensus has not been reached yet on the terminology). Geopolymers are highly coordinated binder systems which have a low calcium content and for which their network almost exclusively consists of aluminosilicate. The network is built out of SiO_4 and AlO_4 tetrahedra linked by sharing oxygen atoms [5-7].

On the other hand, there is a fast-emerging field of study that focuses on how to modify the final physicochemical properties of cementitious materials using nanotechnology. Synthesis and assembly of materials in the nanometer scale range offer the possibility for development of new cement additives such as novel superplasticizers, nanoparticles, or nano-reinforcements [8,9]. Due to their ultrafine size, nano-particles possess unique physical and chemical properties not found in conventional materials and therefore are being applied in many fields to fabricate new materials with novel functions [10]. Relatively small quantities of nanosized materials are sufficient to improve the performance of composites [11]. Nanomaterials applied to cement-based materials are having an incredible impact in the construction field where a huge group of materials have been developed/applied in diverse cementitious systems, such as nano-silica (SiO_2) [12-16], nano-iron oxide (Fe_2O_3) [17-19], nano-titanium oxide (TiO_2) [20-22], nano-alumina (Al_2O_3) [23,24], nano-calcite ($CaCO_3$) [25-27], nanotubes [28,29], nano-clay particles [24,30], among others. In general, nanoparticles can act as the nuclei for cement products to accelerate the cement hydration matrix that densifies the microstructure thereby reducing porosity and permeability [8].

There are several chemistry technologies for the production of nanoparticles. However, numerous researchers prefer the sol-gel technology over other methods to control the material at the atomic scale due to its versatility and high precision in the generation of final products. The sol-gel process involves the conversion of monomers into a colloidal solution (sol) that acts as the precursor for an integrated network (or gel) of either discrete particles or networks [31].

In the last few decades, several researchers have been modifying the sol-gel method to produce nanoparticles by using surface-active substances, also known as surfactants, which preferentially adsorb at the air-liquid, liquid-liquid, or liquid-solid interfaces. Surfactants are generally classified in two types: (1) ionic surfactants and (2) non-ionic surfactants [32]. One of the most commonly used surfactants for the production of calcium-based nanoparticles [31],[33-36] is the non-ionic Triton X-100 surfactant ($C_{14}H_{22}O(C_2H_4O)_{10}$) which is composed of a neutral head group, often compiled by a hydroxyl group, and a hydrophobic body. Triton X-100 is adsorbed on the surface of the primary $Ca(OH)_2$ nanoparticles due to the hydrogen bonds between the hydroxyl group (OH^-) and the -O of the polyoxyethylene group of Triton X-100, forming a steric barrier [37]. Therefore, the surfactant micelles formed in aqueous systems can encapsulate the calcium species and maintain well dispersed particles during the sol production step of the sol-gel process. The micelles can prevent the gelation step by restricting the growth, the agglomeration, and/or the precipitation of the particles by a particle size control under specific experimental conditions such as concentration, pH, temperature, and stirring rate.

 doi:10.20944/preprints202304.1079.v1

Thus, the sol-gel method modified by surfactants is a good technique to produce well dispersed calcium nano-systems capable of being used in AAMs field.

On the other hand, $Ca(OH)_2$ has been used as a common activator of aluminosilicates like blast furnace slag, fly ash, and also has been applied to materials such as metakaolin [38],[39]. An advantage of this activator is its low cost compared to compounds based on sodium and potassium. On the global market, the cost of calcium hydroxide is at least five to six times lower than the cost of sodium hydroxide [38]. Therefore, diverse researchers have been investigating the use/application of different types of calcium nanoparticles in cementitious systems to generate physicochemical alterations of their final structures where some of the most interesting results have included the production of additional calcium-silicate hydrate (C-S-H) and calcium aluminosilicate hydrate (C-A-S-H) gels with a direct impact in the properties of the final cementitious systems [25],[40],[41]. It is important to mention that the nanostructure of cementitious gels, e.g. alkali-activated aluminosilicates products, cannot be readily characterized due to their amorphous nature and the complex multiphases system generated due to their chemical composition [42]. Regularly, the AAMs/geopolymers binder phases are often assumed to be formed simply by the hardening of the amorphous aluminosilicate gels with no description or analysis of any potential crystallization pathways [43]. However, several authors have been exploring the structure of the gels formed during the alkaline activation of the aluminosilicate's raw minerals and their main reaction products, where in some cases show semi-crystalline order [43],[44].

Kiventerä et al. [45] reported that gold MTs have low reactivity and require the addition of a co-binder to achieve a strong matrix by alkali activation, but this is not an effective method to stabilize poorly reactive gold MTs with low calcium content in its chemical composition; hence, other approaches are needed. The goal of the present study is to investigate the effect of the calcium hydrolyzed nano-solutions in strength and structure of alkali-activated mines tailings. The specific objectives of this study are (a) synthesize and characterize stable nano-solutions rich in calcium hydrolyzed species for use as a calcium resource additive, and also as an additional alkaline solution for gold MT paste formulations, (b) investigate the potentials of the alkaline calcium nano-solutions in modifying the final physicochemical properties of the AAMs, and (c) provide evidences based on the AAM specimens evaluations to understand the generation of the additional cementing binders able to densify the AAMs at nanostructure level due to their role in reducing porosity, which is essential in extending the performance of the AAMs systems.

2. Materials and Methods

2.1. Fourier transform infrared (FTIR) characterization

A Thermo Electron Nicolet 4700 Fourier transform infrared (FTIR) spectrometer was used to collect the spectra in the transmittance mode at specific frequencies ranging from 4000 to 400 cm^{-1}. The FTIR system was equipped with a KBr detector. The resulting spectrum analyses were interpreted to identify the specific functional groups within the analyzed samples.

2.2. Quantitative X-Ray Diffraction (QXRD) characterization

XRD analysis was performed to investigate the phase composition of the MT and the AAMs systems. Measurements were made using an X'Pert PRO MPD x-ray diffraction system. The x-ray radiation was Cu Kα, λ = 1.5418 Å and the current was 40 mA with a tension of 45 kV. The scan time and instrument parameters were identical for all the samples with a 2θ angle range between 10° and 90°. To perform the QXRD analysis for the AAMs specimens the X'Pert HighScore software, which includes the Rietveld method

 doi:10.20944/preprints202304.1079.v1

[46,47], was used. The internal standard material added was 9.1 wt.% of synthetic diamond with particle sizes between 2-4 μm [48,49]. The samples were prepared by intergrading each one of them with synthetic diamond using a porcelain mortar. Finally, the powder diffraction file (PDF) codes (International Centre for Diffraction Data - ICDD) were used to identify the crystalline phases.

2.3. Uniaxial Compressive Tests

The compressive strength of the reacted MT samples was tested following ASTM C109. The MTS Landmark 370.10 machine at a constant displacement rate of 0.21 mm/min was used to evaluate the different AAMs systems. The cubic samples cured for seven days were first placed between two metallic plates to assure that the surfaces were sufficiently flat for the compression test. In this given experimental condition, a total of three cubes/measurements were taken and averaged.

2.4. Scanning Electron Microscopy/Energy Dispersive Spectroscopy (SEM/EDS) characterization

After the uniaxial compression test, the reacted MT samples were characterized using a FEI QUANTA 600i Environmental SEM which uses a tungsten filament and is equipped with an EDAX Element SDD EDS detector. The semiquantitative chemical composition was reported by averaging ten measurements for each specimen. The morphology of the fracture surface of each sample specifically without being polished was determined.

2.5. High Resolution Transmission Electron Microscopy (HR-TEM) characterization

The calcium-hydrolyzed nano-solutions were characterized by High Resolution Transmission Electron Microscopy (HR-TEM), using a FEI Titan 80-300 microscope able to generate selected area electron diffraction (SAED) patterns and qualitative chemical analysis by Energy Dispersive Spectroscopy of X-Rays (EDS). In addition, Fast Fourier Transformed (FFT) analyses were carried out for atomic planes identification on specific areas of the synthetized nanostructures. These analyses were performed to confirm the shape, size, and chemical composition of the nanoparticles and their structural phases in order to identify the presence of $Ca(OH)_2$ nanocrystalline particles.

2.6. Nitrogen Adsorption-desorption analyses

Nitrogen adsorption analyses were performed using a Micromeritics ASAP 2020 Plus machine. Before the experiments, the samples were degassed under vacuum at 70°C for 24 h. The pore size distribution was calculated by the Barrett, Joyner, and Halenda (BJH) method based on the desorption branches of Nitrogen isotherms. In addition, the Halsey-Faas correction was used, and this procedure gives the dV/dD incremental pore volume (units of $cm^3/g/A$) for each sample evaluated. The specific surface areas were calculated using Brunauer-Emmett-Teller (BET) theory of single-layer adsorption for all samples studied.

2.7. Synthesis of the calcium-hydrolyzed nano-solutions

In this study calcium nitrate tetrahydrate [$Ca(NO_3)_2{\cdot}4H_2O$] 98% extra pure (Acros Organics), ammonium hydroxide [NH_4OH] 28-30% (VWR Chemicals), and Triton® X-100 BP151-100 electrophoresis were used for the synthesis of the calcium hydrolyzed nano-solutions. Diverse past studies have addressed the synthesis and characterization of calcium hydroxide nanoparticles obtained by sol-gel from salt solutions; and most of these studies were concerned with hydroxides and the effects of temperature, pH, ionic concentration, and the type of surfactant. High temperature has been shown to be necessary in

Preprints (www.preprints.org) | NOT PEER-REVIEWED | Posted: 27 April 2023 doi:10.20944/preprints202304.1079.v1

order to obtain very fine particles while the properties of the inorganic materials synthesized strongly depend on the conditions of the environment in which they are generated [50]. Basically, in this study, calcium nitrate tetrahydrate was dissolved in deionized water with a solution temperature of 90°C, and was stirred for 30 to 45 min. Simultaneously, a 10 ml solution of Triton X-100 surfactant was prepared using the double value of the Triton X-100 critical micelle concentration (CMC) and was slowly stirred at 25°C for 30 min. Then, the surfactant solution was added drop-by-drop to the previous calcium solution. This new mixture was allowed to stabilize under continuous stirring for 30 to 45 min until the solution temperature reached 40°C. Depending on the concentration of the calcium nitrate tetrahydrate in the solution, the pH of this first "Sol 1" was between 3 and 5. Finally, a few drops of the diluted NH_4OH solution were added to the previous "Sol 1" until it reached a final pH between 8 and 8.5; and this final solution was called "Sol 2" (Figure 1).

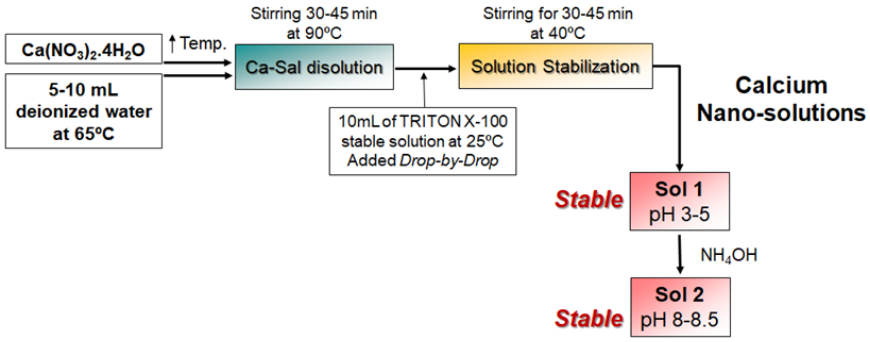

Figure 1. Calcium-hydrolyzed nano-solutions synthesis procedure.

2.8. Alkaline activation process of MTs samples

The pastes were made by mixing the gold MTs and NaOH solutions with a molarity of 10M. Before pastes production began, the raw MT minerals were crushed and sieved to control the particle size to those passing the 30 mesh. The NaOH solutions were prepared by mixing water with NaOH pellets at 97% purity (Sigma-Aldrich) according to a previous study by Zhang et al. [51]; and the solutions then were placed in room temperature (21±1°C) for 30 min to dissipate the heat generated during dissolution. For the case where the calcium nano-systems were used, a secondary solution of well dispersed calcium hydrolyzed nanoparticles were atomized on the previously prepared MT pastes, and well mixed for 10 min to ensure a uniform final paste mixture. The pastes were placed in cubic molds and compacted into three different layers by using the Harvard miniature compaction (HMC) tamper. Each layer was tamped 71 times, which was calculated as equivalent to the HMC mold such that the numbers per unit cross-sectional area was constant. WD-40 lubricant was used to release the samples from the molds. The water/mass ratio used for the original AAM and the AAMs with Ca nanoparticles samples were 0.18 and 0.17, respectively.

The cubic samples were demolded, put in containers, and covered with plastic wrapping to avoid water evaporation during the curing step and then placed in an oven with a slightly elevated temperature of 40±1°C for 24 hours. After that, the oven temperature was increased to 70±1°C for three days. After four days curing, the plastic wrapping was removed, and the specimens were placed in the oven for another three days for drying at the same temperature of 70±1°C. A total of three cubic specimens for each system in the study were cast not only to test the compressive behavior but also to characterize these systems.

3. Results and Discussion

Preprints (www.preprints.org) | NOT PEER-REVIEWED | Posted: 27 April 2023 doi:10.20944/preprints202304.1079.v1

3.1. Raw materials characterization

Gold MTs sample from Vitor (Arequipa, Perú) were used in this study. The geotechnical characterizations of this MTs have been reported in previous works [52,53] and a summary of their characteristics are listed as follows: (1) the mean particle size D_{50} = 0.086 mm with a fine's percentage equal to 41.16% and (2) a coefficient of uniformity Cu = 5.05. The MTs were classified as silty sand (SS) with low plasticity according to USCS classification standards, having a low liquid limit (23.08%), low plasticity (PI = 1.34%), and low capacity for holding water (A = 0.033) [52,53].

The SEM and the EDS semiquantitative chemical composition analyses of the gold mine tailing (Vitor) are shown in Figure 2. The mine tailing SEM micrograph exhibits the typical microstructure of particles with different angularity and finer particles attached to the surface of the coarse particles. The EDS semiquantitative chemical composition indicates the silicon (Si) as primary element of composition in this gold mine tailings, where aluminum (Al), and iron (Fe) are the majority secondary elements, and magnesium (Mg), calcium (Ca), potassium (K), and sodium (Na) are present in minor quantities.

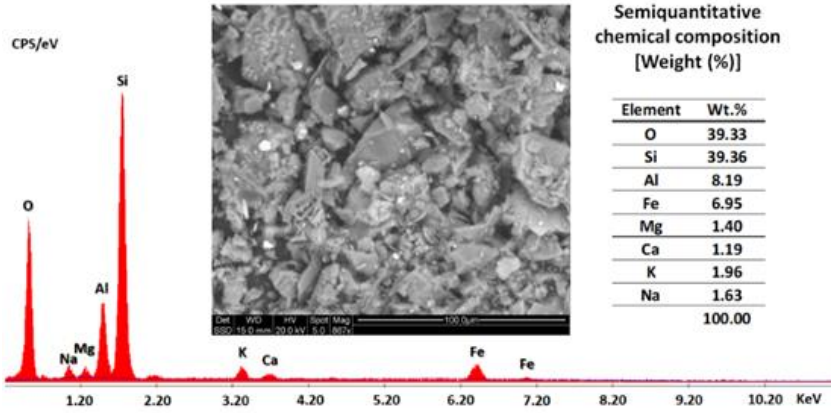

Figure 2. SEM and EDS semiquantitative chemical analyses of the gold mine tailing (Vitor).

The quantitative X-ray diffraction data from this gold MTs was also reported in a previous research work [53], the results indicates that the main crystalline mineral phase is namely quartz (SiO_2) - [51,54], following by muscovite ($KAl_2(FOH)_2$ or $(KF)_2(Al_2O_3)_3(-SiO_2)_6$) [51], magnetite ($Fe_3O_4$) [36,55], albite ($Na(AlSi_3O_8)$)[51,54,56], C-A-S-H ($Ca_3Al(Al_3SiO_{10})(OH)_2$) [53], N-A-S-H ($Na_{17.6}(Al_{16}Si_{56}O_{144})(H_2O)_{38.4}$) [53]. Additionally, a percentage of amorphous phase was also identified [53].

3.2. Synthesis of the calcium hydrolyzed nano-solutions

The nano-solutions synthesis methodology discussed in Section 2.7 is focused on the production of well dispersed calcium hydrolyzed nanoparticles in suitable alkaline aqueous solutions that is compatible with the gold MT alkaline activation process using the NaOH solution as activator. Therefore, the effect of the synthesis parameters (e.g. temperature, pH, and concentration) were analyzed in great detail. For example, the experimental procedure shown in Figure 4 revealed that the temperature of the reaction for the calcium solutions must be equal to or higher than 60°C; otherwise, it is not possible to obtain the water molecular separation from the $Ca(NO_3)_2{\cdot}4H_2O$ according to the following chemical reaction (Eq. 1):

$$Ca(NO_3)_2 \cdot 4H_2O \xrightarrow{\Delta} Ca(NO_3)_2 + 4H_2O \quad (60 - 100°C) \tag{1}$$

Preprints (www.preprints.org) | NOT PEER-REVIEWED | Posted: 27 April 2023 doi:10.20944/preprints202304.1079.v1

After the molecular decomposition of the Ca precursor, the hydrolysis step of the calcium species starts as the pH and the solution temperature were changed. Finally, a stable transparent calcium nano-solution is obtained at pH 8.5, and the product was characterized by different methods.

3.2.1. FTIR of calcium hydrolyzed nano-solutions

The FTIR spectrum in Figure 3 was obtained from a transparent nano-solution at pH = 8.5 where the calcium species were still in a hydrolyzed state in the solution and were confined into the surfactant micellar system. The data presented below refer to the ionic interactions between the hydrated Ca^{+} and the NO_3^- ions in the solution [57].

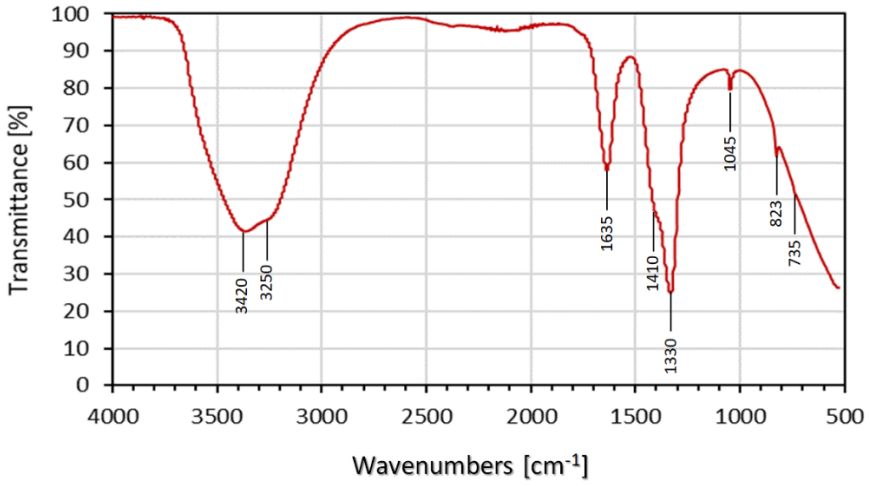

Figure 3. FTIR spectrum from calcium hydrolyzed nano-solution at pH = 8.5

The FTIR spectrum shows the characteristic peaks of water at 3250-3420 cm^{-1} as well as at 1635 cm^{-1} due to the hydroxyl (O-H) stretching and bending modes [58-59]. The presence of the O-H group was caused by the water from the calcium hydrolyzed aqueous nano-solutions [58]. During the process of calcium hydrolyzed nano-solutions synthesis, ammonium nitrate (NH_4NO_3) was generated as a byproduct, and it remains dissolved into the aqueous medium according to the following reaction (Eq. 2):

$$Ca(NO_3)_2 \cdot 4H_2O + 2NH_4OH \rightarrow Ca(OH)_2 + 2NH_4NO_3 + 4H_2O \quad (2)$$

The signals between 1300 and 1500 cm^{-1} correspond to the asymmetric deformation mode of the NH_4^+. It also was possible to determine two simultaneous vibrations associated to the asymmetric stretching and possible in-plane deformation modes of the NO_3^- species. In addition, a totally symmetric stretching mode of the NO_3^- was identified at 1045 cm^{-1}; and at 823 cm^{-1} it was possible to identify the out-of-plane deformation mode from the NO_3^- [57,60]. The low intensity signal at 735 cm^{-1} supports the theory of an ionic interaction, which according to Irish et al. [57], is due to the perturbation between one calcium ion and one nitrate ion that corroborates the simultaneous presence of both species in the nano-solutions at pH = 8.5. Therefore, the calcium hydrated nano-solution at pH 8.5 contains as the principal compound a mixture of calcium hydrolyzed species with a very low population of crystalline $Ca(OH)_2$ nanoparticles, which normally are obtained at higher alkaline pH solutions [31]. At pH values equal or higher than 12, the $Ca(OH)_2$ precipitates due to an increase in the particle size of the calcium hydrated species during the hydrolysis step, which is a non-desirable effect in the current research work. A balance of diverse calcium species in water, such as Ca^{+2}, $Ca(OH)^+$ and $Ca(OH)_2$ [61], thus was expected. Additionally, in the concentrated calcium nano-solutions, the solvated nitrate ion shares

 doi:10.20944/preprints202304.1079.v1

water molecules with the solvated calcium ions, which could generate a potential interaction between the calcium-H_2O-nitrate species [57].

3.2.2. HR-TEM of calcium hydrolyzed nano-solutions

The HR-TEM results are shown in Figure 4 with their corresponding SAED patterns, their elemental chemical analysis by EDS, and the FFT image obtained to distinguish the crystalline structure of the nanoparticles observed from the calcium hydrolyzed nano-solution at pH 8.5. These analyses were performed to confirm the shape, size, and chemical composition of the nanoparticles and their structural phases in order to identify the presence of $Ca(OH)_2$ nanocrystalline particles that corroborates the FTIR results.

Figure 4a shows the distribution of the spherical particles with a variant particle size distribution. The diameters of the particles were lower than 80 nm. The spherical morphologies indicate the effect of the non-ionic surfactant when it reached the CMC that allows the micelles formation to provide a well dispersed system of particles in the aqueous solution, and a direct control in the growing of $Ca(OH)_2$ crystals by encapsulating the calcium hydrolyzed species. Well dispersed nanoparticles production based on a self-assembled molecular cluster system (micelles) in aqueous solutions has been reported in the past by several researchers [33],[34],[61]. Furthermore, Paradles [35] indicated that under controlled experimental parameters, the non-ionic Triton X-100 surfactant produced micelles with a radius of 5.1 nm in aqueous solutions. However, it is expected that the micelles radius could change due to the effect of different conditions, such as pH, temperature, chemical species concentration, stirring rates, type of solvent, among others. One of the factors that could have affected the micelles size in this study was the change of the solution temperature during the synthesis process. Basically, during the calcium hydrolyzed nano-solutions production, the temperature changed from room temperature to 90°C when the surfactant solution was incorporated drop-by-drop under constant stirring. This abrupt temperature change may increase the radius of the micelles according to Paradles [35].

On the other hand, it can be seen that the micelle spherical particles are filled with smaller particles. Thus, Figure 4c shows a higher magnification of the micellar internal structure, which corroborates the presence of nanoparticles with very homogenous particle sizes that are less than 10 nm. Bright electron diffraction spots can be seen in the SAED diffraction pattern, indicating that the internal structure of the micelle spherical particles was formed by polycrystalline nanoparticles with a chemical composition of calcium (Ca), oxygen (O), and nitrogen (N) as shown in the EDS spectra in Figure 4b. The nitrogen (N) signal was expected due to the used calcium salt precursor during the calcium hydrolyzed nano-solutions synthesis step.

Figure 4d, which is a magnification of Figure 4c, shows that some of the hexagonal particles developed well defined edges which illustrates the crystal growth pattern common to $Ca(OH)_2$. In addition, some particles show ends that are fragmented or incomplete because the nano-solutions did not reach the high pH ≈ 12 in which all $Ca(OH)_2$ particles are expected to complete their hydrolysis step that allows their growth and precipitation.

Preprints (www.preprints.org) | NOT PEER-REVIEWED | Posted: 27 April 2023 doi:10.20944/preprints202304.1079.v1

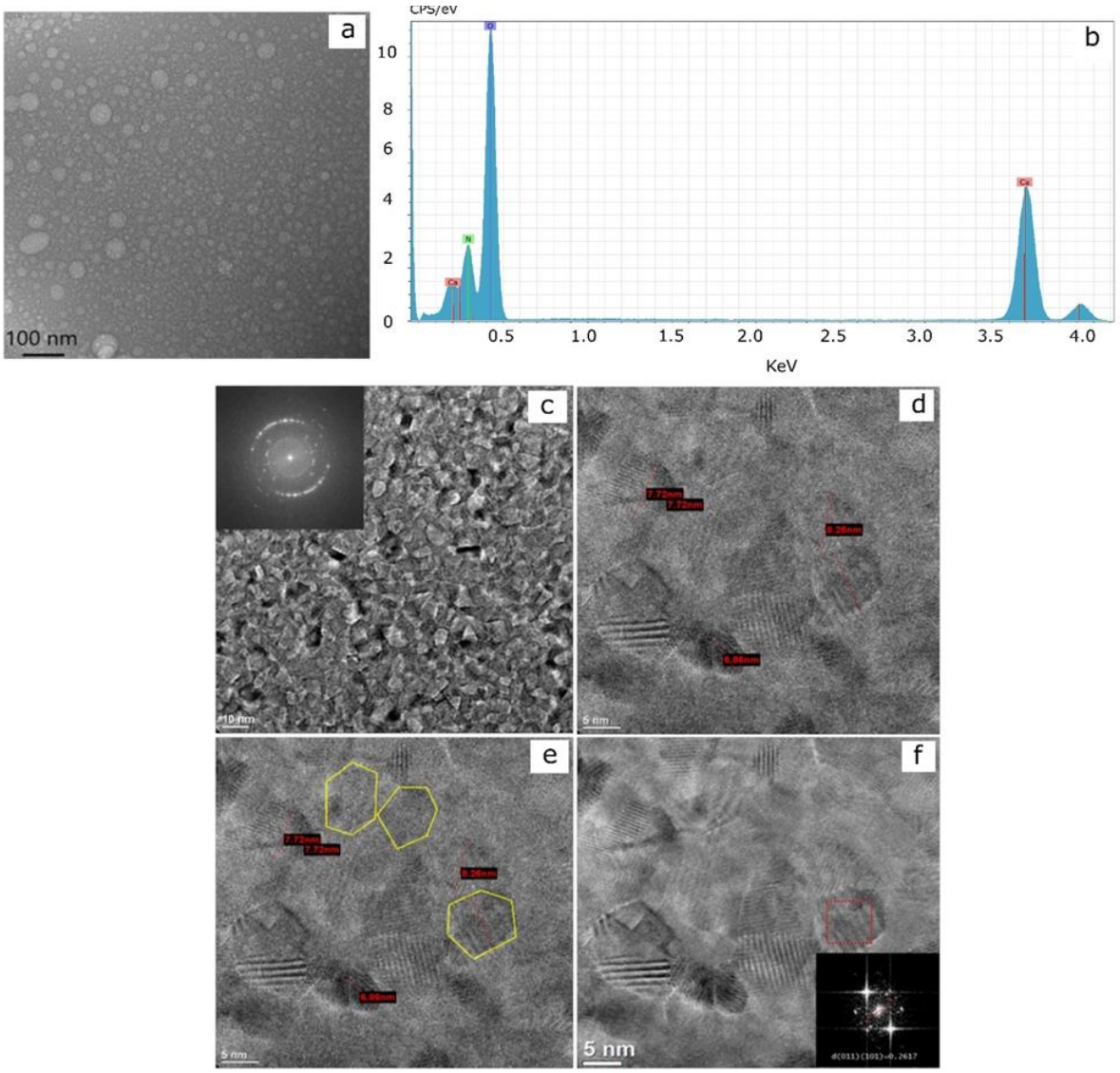

Figure 4. HR-TEM micrographs from calcium hydrolyzed nano-solution at pH = 8.5: (a) general view of the systems conformed by well dispersed spherical particles; (b) qualitative chemical analysis by EDS of the systems shown in a; (c) detail of the internal structure from the spherical particles shown in (a) and its SAED pattern; (d) high resolution image from (c) and measurement of the hexagonal-like particles sizes; (e) highlight of hexagonal-like particles shown in (d); and (f) FFT image from a single-hexagonal particle as identified in (e).

Separated individual $Ca(OH)_2$ tetrahedral crystals clearly are highlighted in Figure 4e with particle sizes lower than 10 nm. These smaller particles with the higher hexagonal symmetry of the $Ca(OH)_2$ crystals are generated when temperatures higher than 60°C are used during the dissolution of the calcium nitrate tetrahydrate in water at the first step of the nano-solution production, which also was reported by Ambrosi et al. [31] who used temperatures close to 90°C during the synthesis process of $Ca(OH)_2$ nanoparticles [31]. Additionally, Michalopoulou et al. [37] indicated that the use of non-ionic Triton X-100 during the production of the dispersed nano-lime [$Ca(OH)_2$] in water resulted in plate-like $Ca(OH)_2$ nanoparticles, which are customarily hexagonal, thereby showing the direct effect of the smaller size, enhanced width, and more angular shape. The reduced size of the nanoparticles was attributed to the reported interaction between Ca^{2+} and the functional group $-CH_2-CH_2-O-$ of Triton X-100, which has been proven to inhibit the growth of the primary particles and the presence of aggregation phenomena.

Table 1. Theoretical and experimental interplanar distances (d_{hkl})

Preprints (www.preprints.org) | NOT PEER-REVIEWED | Posted: 27 April 2023 doi:10.20944/preprints202304.1079.v1

	Portlandite (Space group: P-3m1)	
(hkl)	**Experimental d_{hkl} (nm)**	**Theoretical d_{hkl} (nm)**
(011)	0.2617	0.2685
(101)	0.2617	0.2685

In order to verify the crystalline structure inside the hexagonal particles, an FFT analysis on the HR-TEM micrograph was performed. Figure 4f shows a very clear hexagonal particle (left-bottom) that is highly ordered, and its FFT image shows well defined spots. By measuring the interplanar distances (d_{hkl}), planes (011) and (101) of portlandite [$Ca(OH)_2$] were identified. Based on the XRD pattern, plane (011) has a direct correspondence with the most intense XRD signal at $2\theta = 34.11°$, and plane (101) belongs to the same plane family as shown in Table 1. These results corroborated the presence of portlandite [$Ca(OH)_2$] crystalline particles in the nano-solutions.

3.3. Production and Characterization of the AAMs systems

3.3.1. Compressive strength of the AAMs systems

The uniaxial compression tests of the AAMs specimens were performed after seven days of curing process. The compressive strength average values for all the evaluated systems are reported in Figure 5. It can be seen that the compressive strength of the original AAM cubes was achieved at 9.38 MPa. The compressive strength for the AAMs samples with calcium hydrolyzed nano-solutions at three different concentrations of 1, 2, and 3 wt.% of MTs increased for all the samples as follows: the specimens with 1 wt.% achieved compressive strength of 13.48 MPa, which represents an increase of 44%; for specimens with 2 wt.% the compressive strength was 13.81 MPa, which corresponds to an increase of 47%; and the specimens with 3 wt.% achieved a compressive strength of 15.16 MPa, which was an increase of 62%.

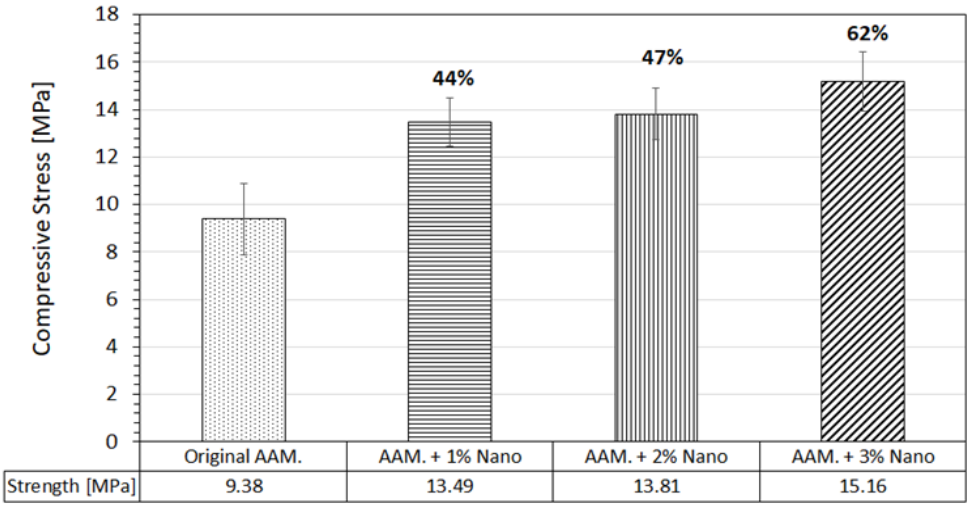

Figure 5. Comparative compressive strength of the original AAM, and the AAMs additivated with calcium hydrolyzed nano-solutions at three different concentrations.

From a chemical reaction standpoint, when an alkaline activator such as sodium hydroxide (NaOH) or potassium hydroxide (KOH) is exposed to aluminosilicate minerals, the phases dissolution starts, and elements such as aluminum and silicon initiate their hydrolysis processes in the presence of an aqueous media rich in OH-, as follows [62]:

$$SiO_2 + 2OH^- \rightarrow [SiO_2(OH)_2]^{2-} \quad (3)$$

Preprints (www.preprints.org) | NOT PEER-REVIEWED | Posted: 27 April 2023 doi:10.20944/preprints202304.1079.v1

$$Al_2O_3 + 3H_2O + 2OH^- \rightarrow 2[Al(OH)_4]^- \quad (4)$$

The addition of calcium hydrolyzed nano-solutions in the low calcium MTs systems provides additional chemical reactions based on the pozzolanic properties of the calcium hydrolyzed nanoparticles disperse in aqueous solutions, which reacts simultaneously with the silicon and aluminum hydrolyzed species generated during the alkaline activation process that affected in a positive way the physicochemical properties of the final AAMs. Some of the additional main products generated in those systems were as follows:

$$[SiO_2(OH)_2]^{2-} + Ca[(H_2O)_6]^{2+} \rightarrow C-S-H_{(gel)} \quad (5)$$

$$[Al(OH)_4]^- + [SiO_2(OH)_2]_2^- + Ca[(H_2O)_6]^{2+} \rightarrow C-A-S-H_{(gel)} \quad (6)$$

It is well known that the C-S-H gel is able to fill the voids and improve the compactness of different cementing systems along with the binding matrix in accordance with Eq. 5 [63,64]. In addition, the C-S-H gel is also generated during the Portland cement hydration process, and it is the main product responsible for the high strength development of this cementing system. Furthermore, it is generally believed that C-S-H gel is the component that strengthens the resulting binder [41]. Additionally, the presence of aluminum (Al) in the system allowed the generation of C-A-S-H gels, which is important in light of the fact that both gels (C-S-H and C-A-S-H) normally non-stoichiometric are among the hydration products of novel AAMs. Hence, the presence of additional calcium species during the MTs alkaline activation step was advantageous because of their role in the formation of hydration products such as C-S-H and C-A-S-H (Eq. 6) gels, which are well-known for the mechanical strength that they impart on cementitious materials [36,64]. Secondaries chemical reactions due to the hydrolysis of other elements, such as magnesium, may take place during the inorganic polymerization process because it easily and drastically reacts with water to form $Mg(OH)_2$, which in the presence of the calcium resource can generate C-M-A-S gel, which can strengthen the microstructure [64]. Chen et al. [65] stated that C-S-H gel may contain Al, Fe, and Mg due to the sorption or co-precipitation processes generated during the hydration process of cementitious materials, where the minor components can modify the crystal growth by substitution in the lattice of the calcium silicate hydrates. On the other hand, Silva de Vargas et al. [66] reported that the matrix formed by alkali-activation of aluminosilicates using the alkaline solution is formed by M-A-S-H gels, where M is the element of the first group of the periodic table (Na^+ and K^+ are the most used).

3.3.2. Quantitative X-ray diffraction (QXRD) analysis of the AAMs systems

Table 2 presents the results of quantitative X-ray diffraction used to identify the mineralogical composition of the original AAM, and the AAMs samples with the added calcium hydrolyzed nano-solutions. The QXRD data using Rietveld refinement method (Table 2) shows that all AAMs samples mainly contain the same crystalline phases as previously identified in the original MTs (section 3.1) except the N-A-S-H phase. The primary crystalline phases are quartz (SiO_2) [36,51,67], albite ($Na(AlSi_3O_8)$)[51,54,56], muscovite ($KAl_2(FOH)_2$ or $(KF)_2(Al_2O_3)_3(-SiO_2)_6$) [51]. However, some additional crystalline phases were detected in low quantities; these phases are magnetite (Fe_3O_4) [36,55], portlandite [$Ca(OH)_2$] [36],[68-71], calcite ($CaCO_3$) [68,69], zeolite [36,69,72,73], C-S-H [68,72,74], and C-A-S-H [70]. The quantification of amorphous phases in each AAMs specimen was also determined.

Table 2. QXRD analyses of all AAMs specimens. Only phases contributing ≥ 0.2 wt.% of the samples are reported.

Preprints (www.preprints.org) | NOT PEER-REVIEWED | Posted: 27 April 2023 doi:10.20944/preprints202304.1079.v1

Phases	PDF Code	Original AAM. wt. %	AAM. + 1%Nano wt. %	AAM. + 2%Nano wt. %	AAM. + 3%Nano wt. %
Quartz	01-077-8621	38.91	37.24	34.76	31.94
Albite	04-017-1022	9.21	8.43	8.13	7.90
Muscovite	00-001-1098	6.32	5.86	4.64	3.10
Portlandite	00-001-1079	-	0.20	0.20	0.20
Calcite	00-024-0027	-	0.20	0.22	0.33
Magnetite	01-075-0449	0.33	0.20	0.20	0.20
Zeolite	01-076-0620	1.20	0.63	0.24	-
C-S-H	01-076-0618	-	0.47	0.56	0.61
C-A-S-H	00-001-1079	0.71	0.83	0.89	0.92
% Amorphous	-	43.07	45.90	50.13	54.72

The muscovite appears to be the main phase able to release the higher quantities of silicon and aluminum species during the alkaline dissolution of minerals, followed by the albite and quartz phases with dissolution rates lower than muscovite [75]. Therefore, it is expected that C-S-H and C-A-S-H phases could be generated due to the combination of soluble Ca^{2+} ions from the calcium hydrolyzed nano-solutions and the silicon and aluminum ions released from the aluminosilicate phases of the MTs precursor during the dissolution step in the presence of the alkali activator solution [74]. In this case, the main reaction product is an amorphous aluminosilicate cementing phase with low crystallization of C-S-H gel which takes up some percentage of Al in its structure for the generation of additional C-A-S-H gel (Eqs. 5 and 6). Although the C-S-H and C-A-S-H phase contents increase as the calcium hydrolyzed nanoparticle concentration increases in the AAMs systems, the low quantity of these phases, as evidenced by the QXRD results, indicates the potential short-range order of the C-S-H and C-A-S-H phases, which is attributed to the possible formation of nanostructured gels.

Additionally, there is a direct increase of the amorphous content as the calcium hydrolyzed nanoparticles concentration increases in the AAMs specimens, indicating the production of more cementing binders in amorphous state [53]. These results suggest that the presence of the calcium hydrolyzed nanoparticles during the MTs alkaline activation process positively contributed to the dissolution of the aluminosilicate phases, allowing for the generation of additional binders that ultimately contribute to the strength increase in the AAMs specimens (Fig. 5). A similar effect was reported by Zhu et al. [76] in the production of alkali-activated metakaolin/slag pastes where the substitution of metakaolin (with very low calcium content) by slag (with high calcium content) increased the reactivity of precursors, contributing to a higher reaction rate and accelerating the geopolymerization process. Similarly, Canfield et al. [77] investigated the role of calcium in blended fly ash geopolymers and found that calcium can act as activator because the calcium species with OH^- raises the pH in local environments which in turn increases dissolution of local aluminosilicate particles and thus increases the extent of the inorganic polymeric structure.

On the other hand, the previous low quantity of $Ca(OH)_2$ particles identified as part of the calcium hydrolyzed nano-solutions (section 3.2.2.) can make a direct contribution of portlandite content in the AAM systems. Likewise, an insignificant amount of calcite ($CaCO_3$) in the AAMs systems was observed possibly due to the reaction of calcium species with the carbon dioxide from air in presence of an aqueous alkali activator [70,78]. Similarly, the presence of zeolite phase was expected in these types of AAM systems. Provis et al. [43] reported that the identification of nanocrystalline zeolitic materials as a significant component of geopolymeric materials, embedded in an alkaline amorphous aluminosilicate gel phase, is not unexpected. In addition, it is well known that the N-A-S-H phase is present in the raw MTs (section 3.1.) and it is a the zeolitic precursor [53]. However, it is

 doi:10.20944/preprints202304.1079.v1

possible to observe that as the calcium hydrolyzed nanoparticles content increased in the AAMs systems, the zeolite formation decreased, indicating the potential preference of these systems to generate other phases over the zeolite in presence of calcium species. Finally, the magnetite phase showed a slow dissolution process during the alkali activation step, allowing the low release iron species to be part of the formed amorphous cementing binders [65].

3.3.3. FTIR characterization of the AAMs systems

The FTIR spectra from the AAMs samples are shown in Figure 6a. The bands observed at 2920 cm^{-1} and 2840 cm^{-1} are attributed to the symmetric and asymmetric stretching of the C-H groups, which possibly proceeds from the WD-40 lubricant used during the demolding step of the cubic sample preparation [79]; and these vibrations also were identified in the original spectra from the surfactant Triton X-100 used during the calcium nano-solutions synthesis. Figure 6b shows a more detailed look at the FTIR spectra in the region of 1550-550 cm^{-1}. The band at about 1420 cm^{-1} was attributed to the stretching vibrations of the C-O bond of the carbonates, likely the sodium carbonates. Despite the fact that special care was taken to avoid carbonation during the experiments, a small number of carbonates occurred due to the reaction of the activator solution of NaOH with the atmospheric CO_2 [70]. The carbonate within the samples also presented a small protrusion at 875 cm^{-1}, which is an out of plane bending of the carbonate group. In addition, the signal between 693-700 cm^{-1} corresponds to the calcium carbonate phase [80] and potentially to the formation of sodium carbonate [81] that corroborated the QXRD results for the $CaCO_3$ generation during the geopolymerization step.

The small band at about 1380 cm^{-1} was assigned to the nitrates that resulted from the preparation method of the calcium hydrolyzed nano-solutions [70]. A moderate intensity band occurred at 835 cm^{-1}, possibly corresponding to the Si-O bond symmetric stretching vibrations [78]. However, this vibration may have overlapped the signal at 830 cm^{-1} assigned to the bending mode of NO_3^- [83,84].

On the other hand, there is a clear overlapping of signals in the range of 1200-800 cm^{-1}. All the spectra presented a huge absorption band in this region, which is typical for aluminosilicate structures and were attributed to the asymmetric stretching vibration of the Si-O-Si and Si-O-Al bonds in $[SiO_4]^{4-}$ and $[AlO_4]^{5-}$ [70]. In addition, other overlapping signal in this region can be attributed to the S-O adsorption band of SO_4^{-2}, pertinent to the formation of the sulfate-based minerals band that occurs around 1020 cm^{-1} [79].

Preprints (www.preprints.org) | NOT PEER-REVIEWED | Posted: 27 April 2023 doi:10.20944/preprints202304.1079.v1

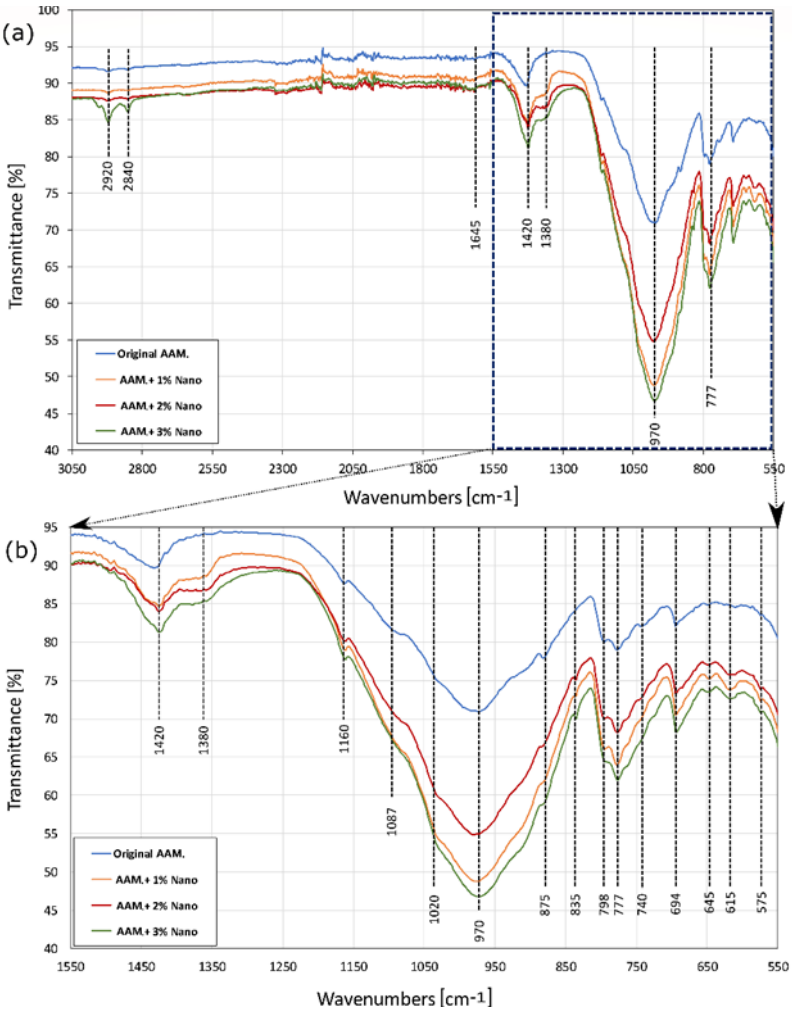

Figure 6. (a) FTIR spectra of the original AAM, and additivated AAMs with calcium hydrated nano-solutions. (b) Zoom in from the wavenumbers' zone between 1550-550 cm^{-1}

The vibration at 798 cm^{-1} is a characteristic signal from quartz, which is the main mineral compound of the used MT, and its presence was also corroborated by the XRD patterns [81]. However, the group of signals at 796 cm^{-1}, 777 cm^{-1}, and 694 cm^{-1} indicate the existence of Si-O-X bonds, which were from the resulting AAMs systems (X stands for tetrahedral silicates or aluminates). The magnitude of the absorption bands is related to the amounts of silicates or aluminates and the degree of the inorganic polymerization [51]. As the concentration of the calcium species increased, there was an increase in the overlapping signal at 740 cm^{-1}; apparently, this band is generated by either one or more of the calcium ions interaction with the nitrate ions [85].

According to Kapeluszna et al. [70], the peaks observed in the 800-600 cm^{-1} zone (645 and 615 cm^{-1}) were distinguishable in the characteristics structure of the C-A-S-H gel vs the Si-O-Si, Al bonds. In addition, the vibrations between 600-400 cm^{-1} (575 cm^{-1}) suggests the occurrence of tetrahedrons in the silicates and aluminosilicates networks in the C-S-H gel and the C-A-S-H gel hydrates [70],[82],[85].

3.3.4. SEM/EDS characterization of the AAMs systems

Figure 7 shows the SEM micrographs from the fractured surfaces of the original and calcium hydrolyzed nano-solution AAMs. These images showed more consolidated structures as the calcium hydrolyzed nano-solutions content increases. It is possible to observe how the irregular shape particles are covered with cementing binders grown over and

 doi:10.20944/preprints202304.1079.v1

between them. Therefore, a densification of the samples is evident as the content of calcium increases in the systems; for instance, the porosity observed in the original AAM systems is filled with a continuous phase of cementing products clearly observed in the SEM images from the AAM with 3% of calcium nanoparticles specimen. Hence, the consolidated microstructure is due to the production of the C-S-H, C-A-S-H, and in major quantity by the amorphous cementing binders that is corroborated by the QXRD results. The chemical compositional maps of the AAMs systems indicate several areas with strong signals of Si, Al, O, and Na, also it was possible to identify secondary elements such as Fe, K, Mg, and Ca.

Table 3. Semiquantitative EDS chemical composition of the AAMs systems

Element	Semiquantitative Chemical Composition [wt.%]			
	Original AAM.	AAM. + 1% Nano	AAM. + 2% Nano	AAM. + 3% Nano
O	36.87	37.89	37.41	39.05
Na	9.23	8.45	8.02	8.05
Mg	0.98	0.83	1.16	1.40
Al	6.76	6.51	6.83	7.53
Si	36.30	37.65	37.12	34.09
K	1.88	1.42	1.56	1.78
Ca	1.48	1.87	2.13	2.37
Fe	6.60	5.37	5.79	5.74

In addition, Si, Al, and O dominated the entire mapped area, indicating their abundance that is expected due to the presence of the aluminosilicate minerals in the MT precursor. The comparative EDS mapping for the specific calcium element distribution (Figure 7) shows no agglomerations of calcium nanoparticles with high dispersion of them into the final consolidated specimens. The increase of Ca signals was directly proportional to the content of the calcium hydrolyzed nanoparticles in the systems. Ca, Si, and Al coexisted in the same area suggesting the homogeneous generation of C-S-H, C-A-S-H and the amorphous binder products [86]. Meanwhile, Fe, K, and Mg also were observed in the same regions as they were part of the original MT precursor. The Sodium shows a strong signal in all the AAMs samples due to its incorporation into the systems when NaOH was used as alkaline solution activator.

The average of ten EDS measurement of different areas from each AAMs specimen is reported in Table 3. These results indicate that the increase of the Ca element content in the AAMs samples was directly proportional to the increase of the calcium hydrolyzed nanosolutions content. Based on the SEM images and EDS analyses (Figure 7), the calcium hydrolyzed nanoparticles had a direct impact in the generation of additional cementing binders that improved the final consolidated microstructure of the AAMs specimens [86].

Preprints (www.preprints.org) | NOT PEER-REVIEWED | Posted: 27 April 2023 doi:10.20944/preprints202304.1079.v1

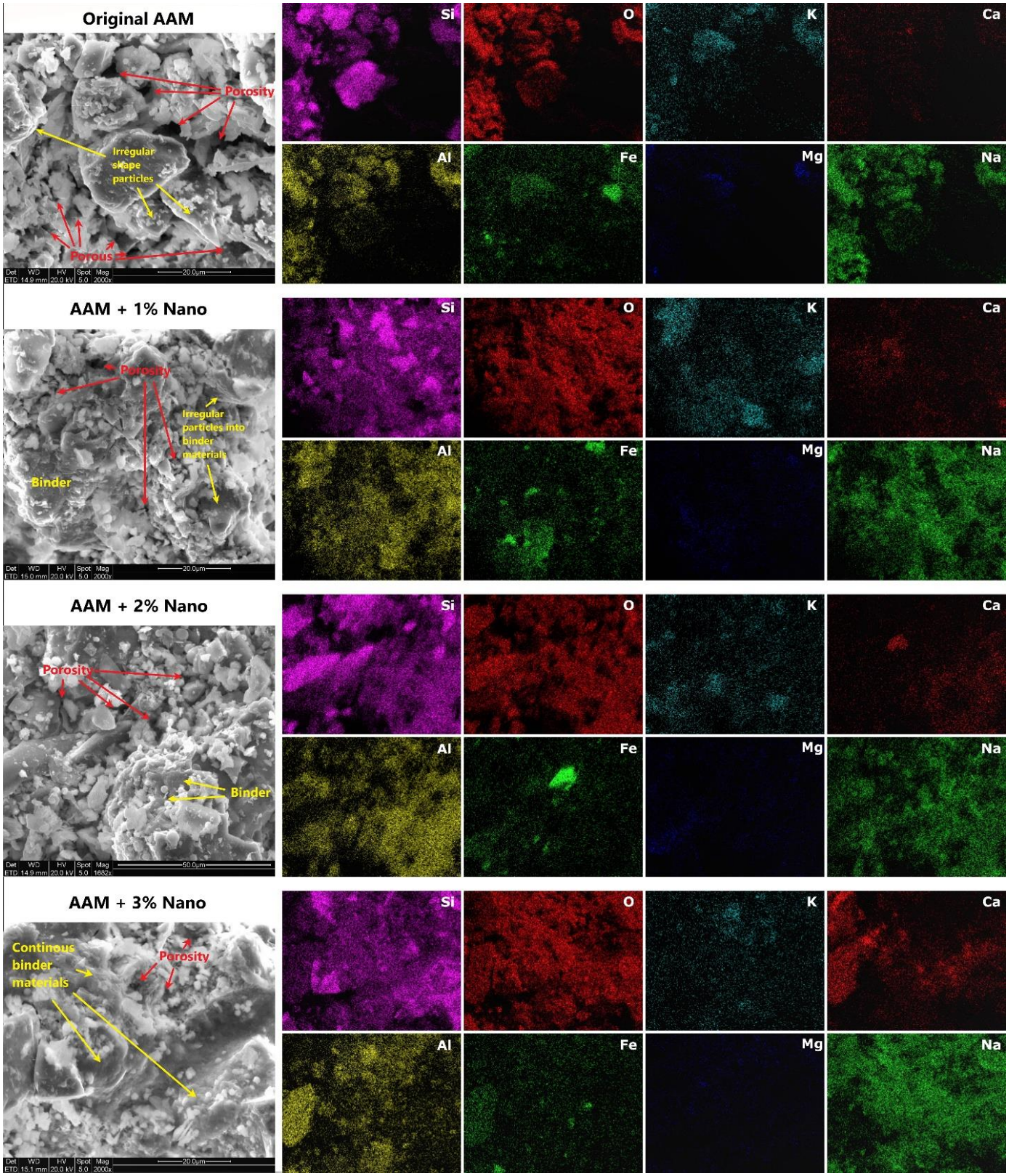

Figure 7. SEM micrographs and EDS elemental mapping analyses of the original AAM, and additivated AAMs with different concentrations of calcium hydrolyzed nano-solutions.

Preprints (www.preprints.org) | NOT PEER-REVIEWED | Posted: 27 April 2023 doi:10.20944/preprints202304.1079.v1

3.3.5. Nitrogen adsorption-desorption analyses of the AAMs systems

The nitrogen adsorption-desorption isotherms and pore size distribution for the original AAM and the additivated AAMs samples with different percentage of calcium hydrolyzed nano-solutions are depicted in Figure 8. According to IUPAC [87], the original AAM sample showed nitrogen adsorption-desorption isotherm typical of type IV (Figure 10a). It means that AAM system exhibits the typical hysteresis loop and has mesopores (2 - 50 nm in diameter). Otherwise, the AAMs additivated with calcium hydrolyzed nano-solutions exhibited isotherm curves conform to type II that means the three systems are non-porous or are defined as macroporous systems (> 50 nm in diameter).

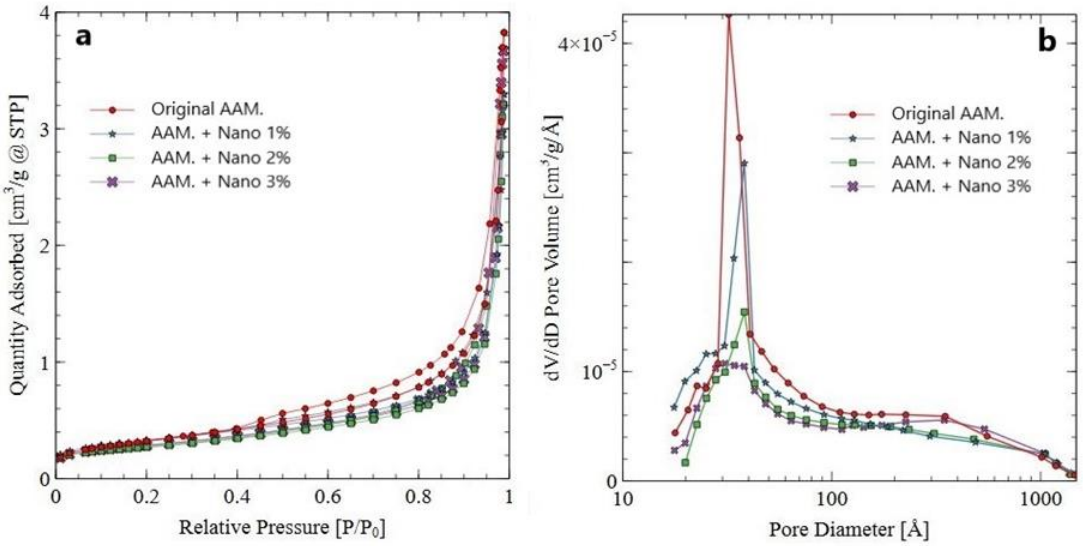

Figure 8. a) Nitrogen adsorption-desorption isotherms, and b) pore size distribution from the original AAM, and the AAMs samples with 1%, 2% and 3% of calcium hydrolyzed nanoparticles.

On the other hand, the BET surface area, average pore diameter and total pore volume deduced from the nitrogen sorption isotherms for these samples are summarized in Table 4. The specific surface area values decrease in the AAM samples as increase the content of calcium in the nano-solutions which indicates a densification of the AAMs systems at nanostructure levels.

Table 4. Comparison of some parameters of the AAM original, and the AAMs additivated with the calcium hydrolyzed nano-solutions.

AAM System [pore range 2-4 nm]	BET surface area (m^2/g)	Average pore diameter (nm)	Total pore volume (cm^3/g) [pores between 2-4 nm] $x10^{-5}$
AAM Original	1.151	3.44	5.21
AAM + Nano 1%	1.119	3.31	5.17
AAM + Nano 2%	0.921	3.25	4.14
AAM + Nano 3%	0.918	3.23	4.19

Additionally, it is possible to observe in Fig. 8b that AAMs samples with the addition of calcium hydrolyzed nano-solutions tend to adsorb less nitrogen gas than the original AAM sample as the percentage of calcium hydrolyzed nano-solutions increase in the AAMs systems, indicating that the pore volume of the additivated AAMs systems become smaller by increasing the calcium hydrolyzed content in the AAMs systems; even though that the average pore diameter for all the AAMs samples are in a range of 3.23 - 3.44 nm (Table 4). These results indicated that the addition of calcium hydrolyzed nano-solutions change the type of porosity and reduce the pore volume of the AAMs systems due to the

 doi:10.20944/preprints202304.1079.v1

generation of additional binders at nanometric level and corroborate the previous results obtained by QXRD, FTIR and SEM/EDS where the formation of nanostructured C-S-H, C-A-S-H, and amorphous phase were identified. Therefore, these additional binders are also filling the porosity at nanostructure levels in the AAMs systems, making them denser and more compact.

4. Conclusions

The application of surfactant (Triton X-100) during the calcium hydrolyzed nano-solutions synthesis process enabled the production of a self-assembled molecular spherical systems (micelles) in aqueous solutions with diameters less than 80 nm that can encapsulate the partially hydrolyzed calcium nanoparticles in a particle size less than 10 nm. The addition of Triton X-100 led to reduction in the size of the nanoparticles and the formation of reduced amounts of $Ca(OH)_2$ nanoparticles hexagonal in shape, which was characterized by an homogeneous particle size distribution. These new well dispersed nano-solutions systems based on encapsulation of calcium hydrolyzed nanoparticles into the surfactant micelles were able to release the smaller nanoparticles into the AAMs pastes by way of a homogeneous distribution of nanoparticles when the nano-solutions were sprayed systematically during the production of the MT pastes.

The calcium hydrolyzed nano-solutions were found to have a direct effect on the dissolution of the aluminosilicate phases from the gold MT precursor, increasing the tetrahedral silicate and aluminate monomers concentration within each sample as calcium content was increased. In addition, the calcium nanoparticles added to the systems participated in the formation of additional amorphous cementing binders with the presence of nanostructured C-S-H and C-A-S-H phases due to the pozzolanic properties of the calcium hydrolyzed nanoparticles that allowed them to react with the hydrated products generated from the gold MTs precursor during its alkaline activation step.

The AAMs specimens with calcium hydrolyzed nanoparticles showed more consolidated microstructures in comparison to the original AAM system. The production of additional amorphous binders due to the reactivity of the MT precursor with the added calcium hydrolyzed nanoparticles improved the final structures at nanometric-level making it homogeneous, more compact, and denser than in the original AAM, which leads to define the AAMs as macroporous systems able to encapsulate the heavy metals presents in the MTs. These results suggest that the additional cementing binders generated at micro- and nanostructure levels are responsible for the strength increases of the final AAMs specimens. This fact was confirmed by the observed increase of the compressive strength between 44 and 62% in comparison to the original AAM system.

5. Patents

Author Contributions: Conceptualization, Y.P.-M.; and A.H.; methodology, Y.P.-M.; and N.Z.; Investigation, Y.P.-M.; and E.S.-S; validation, Y.P.-M.; and N.Z.; formal analysis, Y.P.-M.; resources, A.H.; H.G.B.S.; N.T. I.Y.M.; and R.S.C.L.; data curation, Y.P.-M.; N.Z.; C.C.; and E.S.-S; writing-original draft preparation, Y.P.-M.; L.F.; and A.H.; writing-review and editing, Y.P.-M.; L.F.; E.S.-S; and A.H.; supervision, A.H.; project administration, A.H.; and L.F.; funding acquisition, A.H., H.G.B.S., N.T. I.Y.M. and R.S.C.L. All authors have read and agreed to the published version of the manuscript.

Funding: This research received no external funding.

Acknowledgments: The research team gratefully acknowledges the financial support provided by the Universidad Nacional de San Agustín (UNSA) de Arequipa through its Joint Center for Mining Sustainability with the Colorado School of Mines.

Conflicts of Interest: The authors declare no conflict of interest.

6. References

1. Perumal, P.; Kiventerä, J.; Illikainen, M. Influence of alkali source on properties of alkali activated silicate tailings, *Mater. Chem. Phys.* **2021**, *271*, 124932.
2. Gokçe, H.S.; Tuyan, M.; Nehdi, M.L. Alkali-activated and geopolymer materials developed using innovative manufacturing techniques: A critical review, *Constr. Build. Mater*. **2021**, *303*, 124483.
3. Shi, C.; Qu, B.; Provis, J.L. Recent progress in low-carbon binders, *Cem. Concr. Res*. **2019**, *122*, 227-250.
4. Provis, J.L. Alkali-activated materials. *Cem. Concr. Res.* **2018**, *114*, 40-48.
5. Mast, B.; Schroeyers, W.; Pontikes, Y.; Vandoren, B.; Schreurs, S. In *The use of alkali activated materials in nuclear industry, Comprehensive Nuclear Materials,* 2nd ed.; Konings, R., Eds.; Elsevier; 2020, Volume 6, pp. 537-556.
6. Provis, J.L.; Bernal, S.A. Geopolymers and related alkali-activated materials, *Annu. Rev. Mater. Res.* **2014**, *44*, 299-327. https://doi.org/10.1146/annurev-matsci-070813-113515
7. Bernal, S.A.; Provis, J.L. Durability of alkali-activated materials: progress and perspectives. *J. Am. Ceram. Soc.* **2014**, *97*, 997-1008.
8. Sanchez, F.; Sobolev, K. Nanotechnology in concrete - A review, *Constr. Build. Mater.* **2010**, *24*, 2060-2071.
9. Collins, A.; *Nanotechnology Cookbook: Practical, Reliable and Jargon-Free Experimental Procedures*, first Ed., Elsevier Science: England, 2012. Pp. 1-324.
10. Li, H.; Xiao, H-G.; Yuan, J.; Ou, J. Microstructure of cement mortar with nano-particles, *Compos. B. Eng.* **2004**, *352:(2),* 185-189.
11. Sobolev, K.; Flores, I.; Hermosillo, R.; Torres-Martínez, L.M. Nanomaterials and nanotechnology for high-performance cement composites, *ACI Mater.* **2006**, *254*, 93-120.
12. Ji, T. Preliminary study on the water permeability and microstructure of concrete incorporating nano-SiO_2, *Cem. Concr. Res.* **2005**, *35:10*, 1943-1947.
13. Bjornstrom, J.; Martinelli, A.; Matic, A.; Borjesson, L.; Panas, I. Accelerating effects of colloidal nano-silica for beneficial calcium-silicate-hydrate formation in cement, *Chem. Phys. Lett.* **2004**, *39:1-3*, 242-248.
14. Jo, B.W.; Kim, C.H.; Tae, G.H.; Park, J.B. Characteristics of cement mortar with nano-SiO_2 particles, *Constr. Build. Mater.* **2007**, *21:(6)*, 1351-1355.
15. Qing, Y.; Zenan, Z.; Deyu, K.; Rongshen, C. Influence of nano-SiO_2 addition on properties of hardened cement paste as compared with silica fume, *Constr. Build. Mater.* **2007**, *21*, 539-45.
16. Qing, Y.; Zenan, Z.; Li, S.; Rongshen, C. A comparative study on the pozzolanic activity between nano-SiO_2 and silica fume, J Wuhan Univ Technol **2006**, *21*, 153-157.
17. Kani; E.N.; Rafiean; A.H.; Alishah, A.; Astani, S.H.; Ghaffar, S.H. The effects of Nano-Fe_2O_3 on the mechanical, physical and microstructure of cementitious composites, *Constr. Build. Mater.* **2021**, *266*, 121137.
18. Sikora, P.; Horszczaruk, E.; Cendrowski, K.; Mijowska, E. The influence of Nano-Fe_3O_4 on the microstructure and mechanical properties of cementitious composites, *Nanoscale Res. Lett.* **2016**, *11:182*, 2-9.
19. Amer, A.A.M.; Abdullah, N.I. Behavior of Portland Cement pastes admixed with nano-iron oxide at elevated temperature, *Int. Res. J. Eng. Technol.* **2014**, *3:9*, 1473-1487.
20. Li, Z.; Ding, S.; Yu, X.; Han, B.; Ou, J. Multifunctional cementitious composites modified with nano titanium dioxide: A review, *Compos. Part A Appl. Sci.* **2018**, *111*, 115-137.
21. Meng, T.; Yu, Y.; Qian, X.; Zhan, S.; Qian, K. Effect of Nano-TiO_2 on the mechanical properties of cement mortar, *Constr. Build. Mater.* **2012**, *29,* 241-245.
22. Daniyal, M.; Akhtar, S.; Azam, A. Effect of Nano-TiO_2 on the properties of cementitious composites under different exposure environments, *J. Mater. Res. Technol.* **2019**, *8:6*, 6158-6172.
23. Cuenca, E.; D'Ambrosio, L.; Lizunov, D.; Tretjakov, A.; Volobujeva, O.; Ferrara, L. Mechanical properties and self-healing capacity of ultra-high performance fibre-reinforced concrete with alumina nano-fibres: Tailoring ultra-high durability concrete for aggressive exposure scenarios, *Cem Concr Compos.* **2021**, *118,* 103956.
24. Rashad, A.M. A synopsis about the effect of nano-Al_2O_3, nano-Fe_2O_3, nano-Fe_3O_4 and nano-clay on some properties of cementitious materials - A short guide for civil engineers, *Mater. Des.* **2013**, *52*, 143-157.
25. Cosentino, I.; Liendo, F.; Arduino, M.; Restuccia, L.; Bensaid, S.; Deorsola, F.; Ferro, G.A. Nano $CaCO_3$ particles in cement mortars towards developing a circular economy in the cement industry, *Procedia Struct.* **2020**, *26*, 155-165.
26. Wu, Z.; Khayat, K.H.; Shi, C.; Tutikian, B.F.; Chen Q. Mechanisms underlying the strength enhancement of UHPC modified with nano-SiO_2 and nano-$CaCO_3$, *Cem Concr Compos.* **2021**, *119*, 103992
27. Liu, X.; Chen, L.; Liu, A.; Wang, X. Effect of nano-$CaCO_3$ on properties of cement paste, *Energy Procedia.* **2011**, *16*, 991-996.
28. Kim, G.M.; Nam, I.W.; Yang, B.; Yoon, H.N.; Lee, H.K.; Park, S. Carbon nanotube (CNT) incorporated cementitious composites for functional construction materials: The state of the art, *Compos. Struct.* **2019**, *227,* 111244.
29. Andrade-Neto, J. da S.; Santos, T.A.; De Andrade-Pinto, S.; Ribeiro-Dias, C M.; Véras-Ribeiro, D.; Effect of the combined use of carbon nanotubes (CNT) and metakaolin on the properties of cementitious matrices, *Constr. Build. Mater*. **2021,** *271,* 121903.
30. Niu, X-J.; Li, Q-B.; Hu, Y.; Tan, Y.-Sh. Liu, Ch-F. Properties of cement-based materials incorporating nano-clay and calcined nano-clay: A review, *Constr. Build. Mater.* **2021**, *284*, 122820.
31. Ambrosi, M.; Dei, L.; Giorgi, R.; Neto, Ch.; Baglioni, P. Colloidal particles of $Ca(OH)_2$: properties and applications to restoration of frescoes, *Langmuir*. **2001**, *17*, 4251-4255.

32. Nakama, Y.; Surfactants. In Cosmetic Science and Technology: Theoretical Principles and Applications, 1st ed.; Sakamoto, K., Lochhead, R.Y., Maibach, H.I., Yamashita, Y., Eds.; Elsevier, 2017, pp. 231-244.
33. Perera, Y. Preparation of nano-ceramics via aqueous sol-gel method modified with surfactants: An overview, *Mater. Sci. Forum*. **2010**, *644*, 79-84.
34. Taglieri, G.; Daniele, V.; Del Re, G.; Volpe, R. A new and original method to produce $Ca(OH)_2$ nanoparticles by using an anion exchange resin, *Adv. in Nanoparticles*. **2015**, *4*, 17-24.
35. Paradles, H. H. Shape and size of a nonionic surfactant micelle. Triton X-100 in aqueous solution, *J. Phys. Chem*. **1980**, *84*, 599-607.
36. Opiso, E.M.; Tabelin, C.B.; Maestre, Ch.V.; Aseniero, J.P.J.; Park, I.; Villacorte-Tabelin, M. Synthesis and characterization of coal fly ash and palm oil fuel ash modified artisanal and small-scale gold mine (ASGM) tailings based geopolymer using sugar mill lime sludge as Ca-based activator, *Heliyon 7*, **2021**, e06654.
37. Michalopoulou, A.; Maravelaki, P.N.; Kilikoglou, V.; Karatasios, I. Morphological characterization of water-based nanolime dispersions, *J. Cult. Herit.* **2020**, *46*, 11-20.
38. Jeon, D.; Jun, Y.; Jeong, Y.; Oh, J. E. Microstructural and strength improvements through the use of Na_2CO_3 in a cement less $Ca(OH)_2$ - Activated Class F fly ash system, *Cem. Concr. Res*. **2015**, *67*, 215-225.
39. Akturk, B.; Kizilkanat, A.B.; Kabay, N. Effect of calcium hydroxide on fresh state behavior of sodium carbonate activated blast furnace slag pastes, *Constr. Build Mater*. **2019**, *21:2*, 388-399.
40. Yuan, B.; Yu, Q.L.; Brouwers, H.J.H. Assessing the chemical involvement of limestone powder in sodium carbonate activated slag, *Mater Struct*. **2017**, *50:136*, 1-14.
41. Yip, C.K.; Lukey, G.C.; Van Deventer, J.S.J. The coexistence of geopolymeric gel and calcium silicate hydrate at the early stage of alkaline activation, *Cem. Concr. Res*. **2005**, *35*, 1688-1697.
42. Palomo, A.; Krivenko, P.; Garcia-Lodeiro, I.; Kavalerova, E.; Maltseva, O.; Fernández-Jiménez, A. A review on alkaline activation: new analytical perspectives, *Mater. de Construcción*. **2014**, *64(66)*, e022.
43. Provis, J.L.; Lukey, G.C.; van Deventer, J. S. J. Do geopolymers actually contain nanocrystalline zeolites? - A re-examination of existing results, *Chem. Mater.* **2005**, *17*, 3075-3085.
44. Fernández-Jiménez, A.; Puertas, F.; Sobrados, I.; Sanz, J. Structure of calcium silicate hydrate formed in alkaline activated slag. Influence of the type of alkaline activator. *J. Am. Ceram. Soc.* **2003**, *86:8*, 1389-1394.
45. Kiventerä, J.; Sreenivasan, H.; Cheeseman, Ch.; Kinnunen, P.; Illikainen, M. Immobilization of sulfates and heavy metals in gold mine tailings by sodium silicate and hydrated lime, *J. Environ. Chem. Eng*. **2018**, *6*, 6530-6536.
46. Snellings, R.; Salze, A.; Scrivener, K.L. Use of X-ray diffraction to quantify amorphous supplementary cementitious materials in anhydrous and hydrated blended cements. *Cem Concr Res,* **2014**, *64*, 89-98.
47. Haha, M.B.; Weerdt, K. De; Lothenbach, B. Quantification of the degree of reaction of fly ash. *Cem Concr Res,* **2010**, *40:11*, 1620-1629.
48. Williams, R.P.; Riessen, A.V. Determination of the reactive component of fly ashes for geopolymer production using XRF and XRD. *Fuel*, **2010**, *89:12*, 3683-3692.
49. Bokhonov, B.B.; Kato, H. Selective growth of silver particles on the facets of synthetic diamond. *Cryst. Eng. Comm*. **2016**, 18, 7430-7434.
50. Blyszko, J.; Kiernozycki, W.; Guskos, N.; Zolnierkiewicz, G.; Typek, J.; Narkiewicz, U.; Podsiadl, M. Study of mechanical properties of concrete with low concentration of magnetic nanoparticles, J Non Cryst Solids. 2008, 354, 4515-4518.
51. Zhang, N.; Hedayat, A.; Bolaños Sosa, H.G.; J.J. G.E. Salas Álvarez,; Ascuña Rivera V.; González, J. Fracture and failure processes of geopolymerized mine tailings under uniaxial compression, *ARMA 20*. **2020**, *1923*, 1-9.
52. Zhang, N.; Hedayat, A.; Sosa, H. G. B.; Tunnah, J.; Cárdenas, J. J. G.; Álvarez, G. E. S. Estimation of the mode I fracture toughness and evaluations on the strain behaviors of the compacted mine tailings from full-field displacement fields via digital image correlation. *Theor. Appl. Fract. Mech.*, **2021**, *114*, 103014.
53. Perera-Mercado, Y.; Hedayat, A.; Tunstall, L.; Clements, C.; Hylton, J.; Figueroa, L.; Zhang, N.; Bolaños Sosa, H.G.; Tupa, N.; Yanqui Morales, I.; Canahua Loza, R.S. Effect of the Class C Fly Ash on Low-Reactive Gold Mine Tailing Geopolymers. *Polymers* **2022**, *14*, 2809.
54. Matalkah, F.; Soroushian, P. Synthesis and characterization of alkali aluminosilicate hydraulic cement that meets standard requirements for general use, *Constr Build Mater.* **2018**, *158*, 42-49.
55. Perera-Mercado, Y.A.; Betancourt-Galindo, R.; Saucedo-Salazar, E.M.; Puente-Urbina, B.A.; Medellín-Banda, D.I.; Neira-Velázquez, M.G.; Gutierrez-Villarreal, M.H.; García-Rodríguez, S.P. Production of micrometer-sized composite polymer-magnetic spheres using as precursor metallurgical wastes, *Polym. Polym. Compos.* **2014**, *22:4*, 387-392.
56. Hayes, S.M.; Root, R.A.; Perdrial, N.; R.M. Maier, Surficial weathering of iron sulfide mine tailings under semi-arid climate, *Geochim. Cosmochim. Acta.* **2014**, *141*, 240-257.
57. Irish, D.E.; Walrafen, G.E. Raman and Infrared Spectral Studies of Aqueous Calcium Nitrate Solutions. *J. Chem. Phys.* **1967**, *46* 378.
58. Amer, A.A.; El-Didamony, H.; El-Sokkary, T.M.; Wahdan, M.I. Synthesis and characterization of some calcium aluminate phases from nano-size starting materials, *Bol. Soc. Esp. Cerám. Vidr.* **2022**, *61:2*, 6198-106

59. Moreira, A.P.D.; Teixeira, A.M.R.F. An investigation on the formation of calcium naphthenate from commercial naphthenic acid solutions by thermogravimetric analysis, *Braz. J. Pet. Gas*. **2009**, *3:2*, 051-056.
60. Wu, H.B.; Chan, M.N.; Chan, Ch.K. FTIR characterization of polymorphic transformation of ammonium nitrate, *Aerosol Sci Technol*. **2007**, *41*, 81-588.
61. Dua, Y.; Meng, Q.; Hou, R.; Yan, J.; Dai, H.; Zhang, T. Fabrication of nano-sized $Ca(OH)_2$ with excellent adsorption ability for N_2O_4, *Particuology*. **2012**, 10, 737-743.
62. Nawaz, M.; Heitor, A.; Sivakumar, M. Geopolymers in construction - Recent developments, *Constr Build Mater*. **2020**, *260*, 120472.
63. Sumesh, M.; Alengaram, U.J.; Jumaat, M.Z.; Mo, K.H.; Alnahha, M.F. Incorporation of nano-materials in cement composite and geopolymer based paste and mortar - A review, *Constr Build Mater*. **2017**, *148*, 62-84.
64. Tsai, Ch.-J.; Huang, R.; Lin, W.-T.; Wang, H.-N. Mechanical and cementitious characteristics of ground granulated blast furnace slag and basic oxygen furnace slag blended mortar, *Mater. Des.* **2014**, *60*, 267-273.
65. Chen, Q.Y.; Tyrer, M.; Hills, C.D.; Yang, X.M.; Carey, P. Immobilization of heavy metal in cement-based solidification/stabilization: A review, *Waste Manage*. **2009**, *29*, 390-403.
66. Silva de Vargas, A.; Dal Molin, D.C.C.; Masuero, Â.B.; Vilela, A.C.F., Castro-Gomes, J.; De Gutierrez, R.M. Strength development of alkali-activated fly ash produced with combined NaOH and $Ca(OH)_2$ activators, *Cem Concr Compos*. **2014**, *53*, 341-349.
67. Kamath, M.; Prashant, Sh.; Kumar, M. Micro-characterization of alkali activated paste with fly ash-GGBS-metakaolin binder system with ambient setting characteristics, *Constr Build Mater*. **2021**, *277*, 122323.
68. Zhou, Z.; Sofi, M.; Liu, J.; Li, Sh.; Zhong, A.; Mendis, P. Nano-CSH modified high volume fly ash concrete: Early-age properties and environmental impact analysis, *J. Clean. Prod.* **2021**, *286*, 124924.
69. Asikin-Mijan, N.; Taufiq-Yap, Y.H.; Lee, H.V. Synthesis of clamshell derived $Ca(OH)_2$ nano-particles via simple surfactant-hydration treatment, *J. Chem. Eng.* **2015**, *262*, 1043-1051.
70. Kapeluszna, E.; Kotwica, Ł.; Rózycka, A.; Gołek, Ł. Incorporation of Al in C-A-S-H gels with various Ca/Si and Al/Si ratio: Microstructural and structural characteristics with DTA/TG, XRD, FTIR, and TEM analysis, *Constr Build Mater.*; **2017**, *155*, 643-653.
71. Madrid, J.A.; Lanzón, M. Synthesis and morphological examination of high-purity $Ca(OH)_2$ nanoparticles suitable to consolidate porous surfaces, *Appl. Surf. Sci.* **2017**, *424:1*, 2-8.
72. Kouvelos, E.; Kesore, K.; Steriotis, T.; Grigoropoulou, H.; Bouloubasi, D.; Theophilou, N.; Tzintzos, S.; Kanelopoulos, N. High pressure N_2/CH_4 adsorption measurements in clinoptilolites, *Microporous Mesoporous Mater.* **2007**, *99*, 106-111.
73. Montes-Luna, A.J.; Fuentes-López, N.C.; Castruita-de-León, G.; Pérez-Camacho, O.; Yeverino-Miranda, C.Y.; Perera-Mercado, Y.A. Mixed matrix composite membranes for binary (CH_4/N_2) and ternary ($CH_4/N_2/CO_2$) gas separations, *J. Appl. Polym. Sci.* **2020**, *138:14*, 1-9.
74. Falah, M.; Obenaus-Emler, R.; Kinnunen, P.; Illikainen, M. Effects of activator properties and curing conditions on alkali-activation of low-alumina mine tailings, *Waste Biomass Valorization.* **2020**, *11*, 5027-5039.
75. Xu, H.; Van Deventer, J.S.J. The effect of alkali metals on the formation of geopolymeric gels from alkali-feldspars, *Colloids Surf. A Physicochem. Eng.* **2003**, *216*, 27-44.
76. Zhu, H.; Liang, G.; Li, H.; Wu, Q.; Zhang, Ch;. Yin, Z.; Hua, S. Insights to the sulfate resistance and microstructures of alkali-activated metakaolin/slag pastes, *Appl. Clay Sci.* **2021**, *202*, 105968.
77. Canfield, G.M.; Eichler, J.; Griffith, K.; Hearn, J.D. The role of calcium in blended fly ash geopolymers, *J. Mater. Sci*. **2014**, *49*, 5922-5933.
78. Nikolov, A. Physical properties and powder XRD characterization of coal fly ash-based geopolymer heated up to 1150 °C. *Review of the Bulgarian Geological Society*, **2019**; *80:3*, 36-38
79. Allel, A.; Naceur, M.W.; Benguergoura, H.; Ledoux, A.; Saeed, W.Sh.; Al-Odayni, A.B.; Aouak, T. Pervaporative separation of water–ethanol mixtures using an Algerian Na+ montmorillonite nanoclay-incorporated poly(vinyl alcohol) nanocomposite membrane, *RSC Adv*. **2020**, *10*, 39531.
80. Jin, Y.; Stephan, D.; Lu, Z. The effects of calcium formate on the early hydration of alkali silicate activated slag, *Mater Struct.* **2019**, *52*, 37.
81. Sánchez-Sánchez, A.; Cerdán, M.; Jordá, J.D.; Amat, B.; Cortina, J. Characterization of soil mineralogy by FTIR: application to the analysis of mineralogical changes in soils affected by vegetation patches, *Plant Soil*. **2019**, *439*, 447-458.
82. Garcia-Lodeiro; I.; Fernandez-Jimenez, A.; Blanco, M.T.; Palomo, A. FTIR study of the sol-gel synthesis of cementitious gels: C-S-H and N-A-S-H, *J Solgel Sci Technol*. **2008**, *45*, 63-72.
83. Berzina-Cimdina, L.; Borodajenko, N. Research of calcium phosphates using Fourier transform infrared spectroscopy. In: *Infrared Spectroscopy*, 1st ed.; Theophanides T.,Eds.; IntechOpen: London, England, **2012**, pp. 123-149.
84. Castro, P.M.; Jagodzinski, P.W. FTIR and Raman spectra and structure of $Cu(NO_3)^+$ in aqueous solution and acetone, *Spectrochim Acta A Mol Spectrosc*. **1991**, *47:12*, 1707-1720.
85. Koohestani, B.; Mokhtari, P.; Yilmaz, E.; Mahdipour, F.; Darban, A.K. Geopolymerization mechanism of binder-free mine tailings by sodium silicate, *Constr Build Mater*. **2021**, *268:25*, 121217.

 doi:10.20944/preprints202304.1079.v1

86. Temuujin, J.; Van Riessen, A.; R. Williams, Influence of calcium compounds on the mechanical properties of fly ash geopolymer pastes, *J. Hazard. Mater*. **2009**, *167*, 82-88.
87. Rouquerol, J., Rouquerol, F., Llewellyn, P., Maurin, G. and Sing, K.S.W. *Adsorption by Powders and Porous Solids: Principles, Methodology and Applications*, 2nd ed.; Academic press: New York, US, **2013**. pp. 107–110.